

Fault-tolerant control of an error-corrected qubit

<https://doi.org/10.1038/s41586-021-03928-y>

Received: 23 September 2020

Accepted: 18 August 2021

Published online: 4 October 2021

 Check for updates

Laird Egan^{1,2,10}✉, Dripto M. Debroy^{4,11}, Crystal Noel^{1,2}, Andrew Risinger^{1,2,3}, Daiwei Zhu^{1,2,3}, Debopriyo Biswas^{1,2}, Michael Newman^{5,11}, Muyuan Li^{6,7}, Kenneth R. Brown^{4,5,6,7,8}, Marko Cetina^{1,2} & Christopher Monroe^{1,2,3,4,5,9}

Quantum error correction protects fragile quantum information by encoding it into a larger quantum system^{1,2}. These extra degrees of freedom enable the detection and correction of errors, but also increase the control complexity of the encoded logical qubit. Fault-tolerant circuits contain the spread of errors while controlling the logical qubit, and are essential for realizing error suppression in practice^{3–6}. Although fault-tolerant design works in principle, it has not previously been demonstrated in an error-corrected physical system with native noise characteristics. Here we experimentally demonstrate fault-tolerant circuits for the preparation, measurement, rotation and stabilizer measurement of a Bacon–Shor logical qubit using 13 trapped ion qubits. When we compare these fault-tolerant protocols to non-fault-tolerant protocols, we see significant reductions in the error rates of the logical primitives in the presence of noise. The result of fault-tolerant design is an average state preparation and measurement error of 0.6 per cent and a Clifford gate error of 0.3 per cent after offline error correction. In addition, we prepare magic states with fidelities that exceed the distillation threshold⁷, demonstrating all of the key single-qubit ingredients required for universal fault-tolerant control. These results demonstrate that fault-tolerant circuits enable highly accurate logical primitives in current quantum systems. With improved two-qubit gates and the use of intermediate measurements, a stabilized logical qubit can be achieved.

Quantum computers are promising for solving models of important physical processes, optimizing complex cost functions and challenging cryptography in ways that are intractable using current computers^{8–12}. However, realistic quantum component failure rates are typically too high to achieve these goals^{13,14}. These applications will therefore almost certainly require quantum error-correction schemes to greatly suppress errors^{4,6}.

Quantum error-correcting codes combine multiple physical qubits into logical qubits that robustly store information within an entangled state^{1,2,15}. However, these codes are not enough on their own. Fault-tolerant (FT) operations, which limit the ways in which errors can spread throughout the system, must also be used. Without them, the logical error rate may be limited by faults at critical circuit locations that cascade into logical failures, negating the advantage of error correction.

FT state preparation, detection and operations have been demonstrated using quantum error-detecting codes with four data qubits^{16–20}. These codes can identify when errors have occurred, but do not extract enough information to correct them. There have also been quantum demonstrations of classical repetition codes to correct quantum errors restricted along one axis^{21–26}. In other work, qubits have been encoded into quantum error-correcting codes that can correct all

single qubit errors, but the encoding procedure was not fault tolerant²⁷ and the system was not large enough to measure the error syndromes non-destructively using ancilla^{28,29}. Parallel work on bosonic codes has demonstrated encoded operations^{30,31}, FT detection, and one-axis³² and two-axis^{33,34} error correction on encoded qubits. For both qubit codes and bosonic codes, FT state preparation of a code capable of correcting all single-qubit errors has not been achieved.

Here we demonstrate a quantum error-correcting code with FT control over all of the required operations: state preparation, measurement, logical gates and stabilizer measurement. Unlike previous studies, the code demonstrated here protects against any single circuit fault (along any axis and without postselection), realizing quadratic error suppression in principle. In practice, this error suppression requires high-fidelity components and localized errors to take effect. We observe a logical operation, state preparation and measurement in the Z basis that exceeds the performance of its physical counterpart. More generally, we realize logical primitives that outperform the limiting physical operation used in their construction, namely our native two-qubit entangling gate.

To experimentally verify the properties of fault tolerance, we compare non-fault-tolerant (nFT) preparation, nFT logical gates and nFT stabilizer measurement to their FT counterparts and observe the

¹Joint Quantum Institute, Center for Quantum Information and Computer Science, University of Maryland, College Park, MD, USA. ²Department of Physics, University of Maryland, College Park, MD, USA. ³Department of Electrical and Computer Engineering, University of Maryland, College Park, MD, USA. ⁴Department of Physics, Duke University, Durham, NC, USA. ⁵Department of Electrical and Computer Engineering, Duke University, Durham, NC, USA. ⁶School of Chemistry and Biochemistry, Georgia Institute of Technology, Atlanta, GA, USA. ⁷School of Computational Science and Engineering, Georgia Institute of Technology, Atlanta, GA, USA. ⁸Department of Chemistry, Duke University, Durham, NC, USA. ⁹IonQ, Inc, College Park, MD, USA. ¹⁰Present address: IonQ, Inc, College Park, MD, USA. ¹¹Present address: Google Research, Venice, CA, USA. ✉e-mail: laird.egan@gmail.com

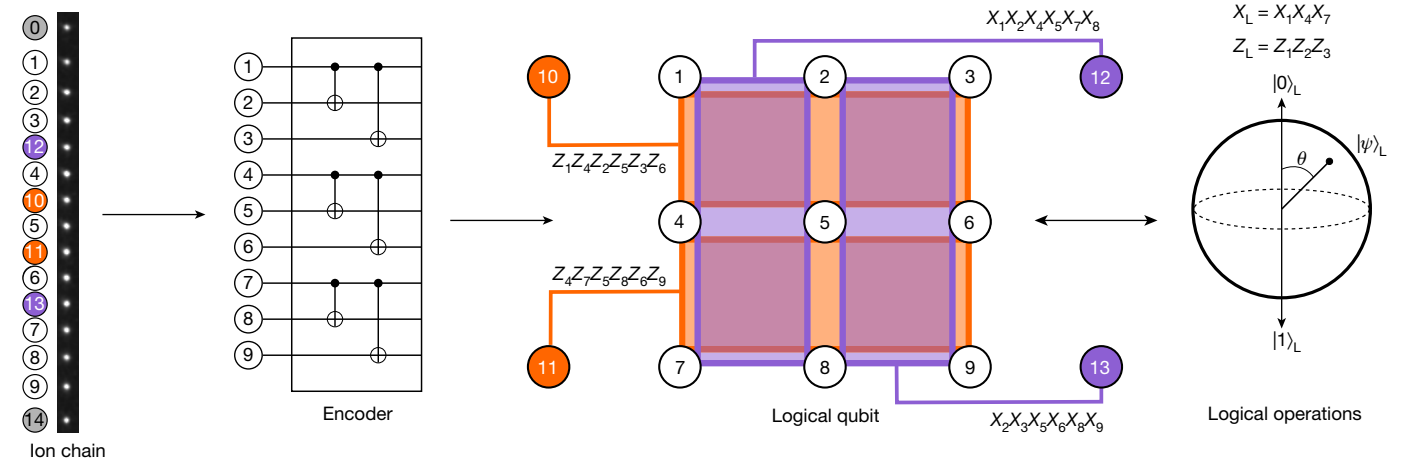


Fig. 1 | The Bacon–Shor subsystem code implemented on a 15-ion chain. Bacon–Shor is a $[[9,1,3]]$ subsystem code that encodes nine data qubits into one logical qubit. Four weight-six stabilizers are mapped to ancillary qubits

reduced suppression of errors. In the process, we generate high-fidelity encoded magic states above the distillation threshold, which are a critical resource for certain universal FT quantum computing architectures⁷.

The quantum computer used in this study consists of laser-cooled ¹⁷¹Yb⁺ ions trapped above a microfabricated chip³⁵ in a room-temperature vacuum chamber. Quantum gates are driven by individually optically addressing up to 32 equispaced ions in a single chain via a multichannel acousto-optic modulator (AOM)³⁶. We implement high-fidelity native single-qubit and two-qubit gates with fidelities of 99.98% and 98.5–99.3%, respectively. All-to-all two-qubit gate connectivity is achieved through coupling of ions via a shared motional bus³⁷. Details of the system, characterization and benchmarking are available in Methods and Supplementary Information.

As shown in Fig. 1, we implement a $[[9,1,3]]$ Bacon–Shor code^{38,39}. As it has distance of three, the code is able to correct any single-qubit error. This code is well suited to near-term ion-trap quantum computing architectures for two reasons. First, Bacon–Shor codes can be prepared fault tolerantly without intermediate measurement. Compared with the typical projective preparation of topological codes, unitary preparation requires fewer gates and fewer ancillary qubits. This allows us to demonstrate FT primitives with fewer resources and without intermediate measurements, with the understanding that intermediate measurements will ultimately be required for algorithmic error suppression. Second, this code choice is a reasonable midpoint between the qubit efficiency of the seven-qubit Steane code and the robustness of the Surface-17 code⁴⁰. Although the Bacon–Shor stabilizers are weight six and non-local, they can be fault tolerantly measured using only one ancilla per stabilizer⁴¹ and leverage the all-to-all connectivity in the device.

As a subsystem code, the Bacon–Shor code is a generalization of Shor’s code¹ that has four additional degrees of freedom known as gauge qubits. For particular choices of gauge, its logical states are products of Greenberger–Horne–Zeilinger (GHZ) states:

$$\begin{aligned}
 |0\rangle_L \otimes |\bar{X}\rangle_G &= \frac{1}{2\sqrt{2}}(|+++ \rangle \pm |--- \rangle)^{\otimes 3}, \\
 |+- \rangle_L \otimes |\bar{Z}\rangle_G &= \frac{1}{2\sqrt{2}}(|000 \rangle \pm |111 \rangle)^{\otimes 3},
 \end{aligned}
 \tag{1}$$

where $|\pm \rangle = (|0 \rangle \pm |1 \rangle) / \sqrt{2}$ and $|\bar{X} / \bar{Z} \rangle_G$ refer to different states of the gauge qubits (Supplementary Information).

Bacon–Shor codes support a wide range of FT operations, including state preparation, state measurement, gates and stabilizer measurement. Fault tolerance, as a design principle, ensures faults on physical operations do not propagate to uncorrectable multiqubit failures in the

10, 11, 12 and 13, for measuring errors in the X and Z basis. We demonstrate encoding of the logical qubit, with subsequent logical gate operations or error syndrome extraction.

circuit. As seen in equation (1), not all Bacon–Shor logical states require global entanglement; it is precisely this construction of decoupled GHZ states that allows Bacon–Shor logical states to be prepared unitarily and fault-tolerantly. In the Z_L / X_L basis, the logical information is encoded redundantly into the relative phase of each state. Although a single circuit fault may corrupt one of the three GHZ states, the information can be recovered from the other two.

FT measurement (in the X/Z basis) is performed by individually measuring the data qubits (in the X/Z basis). From this information, one can recover relevant stabilizer outcomes as correlations among the single data-qubit outcomes. This information is then combined with any previously extracted syndromes, and then collectively decoded to produce an offline correction. It is worth emphasizing that although our system does not currently support intermediate measurements, this offline correction does not differ from the final step of a logical qubit memory experiment with multiple rounds of intermediate measurements.

Fault tolerance in logical gates is often achieved via transversal gates, which are physical operations that act independently on each qubit in a code block. Bacon–Shor codes have transversal constructions, when allowing permutations, for $\{\text{CNOT}_L, H_L, Y_L(\pi/2), X_L\}$ ^{3,42,43}. Here H_L is the logical Hadamard gate and $Y(\theta)$ indicates exponentiation of the Pauli- \bar{Y} matrix, $e^{-i\theta\bar{Y}/2}$, parameterized by the angle θ . FT non-Clifford logical gates, which are required for universality, can be achieved through magic-state distillation⁷.

Finally, measuring error syndromes requires interacting ancillae with multiple data qubits, which could cause damaging correlated errors. However, fault tolerance is achieved by carefully ordering the interactions, so that correlated errors can be reduced to low-weight errors up to a benign transformation of the gauge subsystem^{41,44}.

Encoding the logical qubit

We embed the nine data qubits and four ancilla qubits of the Bacon–Shor-13 code in a single chain of fifteen ions (Fig. 1), with the two end ions left idle to obtain uniform spacing of the central thirteen ions. The mapping of the code onto the chain is chosen to minimize two-qubit gate crosstalk (Supplementary Fig. 5).

The encoding circuit used to create logical states is shown in Fig. 2a. The right subcircuit (blue) is FT because there are no entangling operations between independent GHZ states that would allow errors to propagate; however, it is limited to preparation of only Z- and X-basis states. One may prepend an optional subcircuit (red, dashed) that enables the encoding of arbitrary $|\psi\rangle_L$ states, controlled by a single physical qubit state $|\psi\rangle$. This circuit can produce global entanglement,

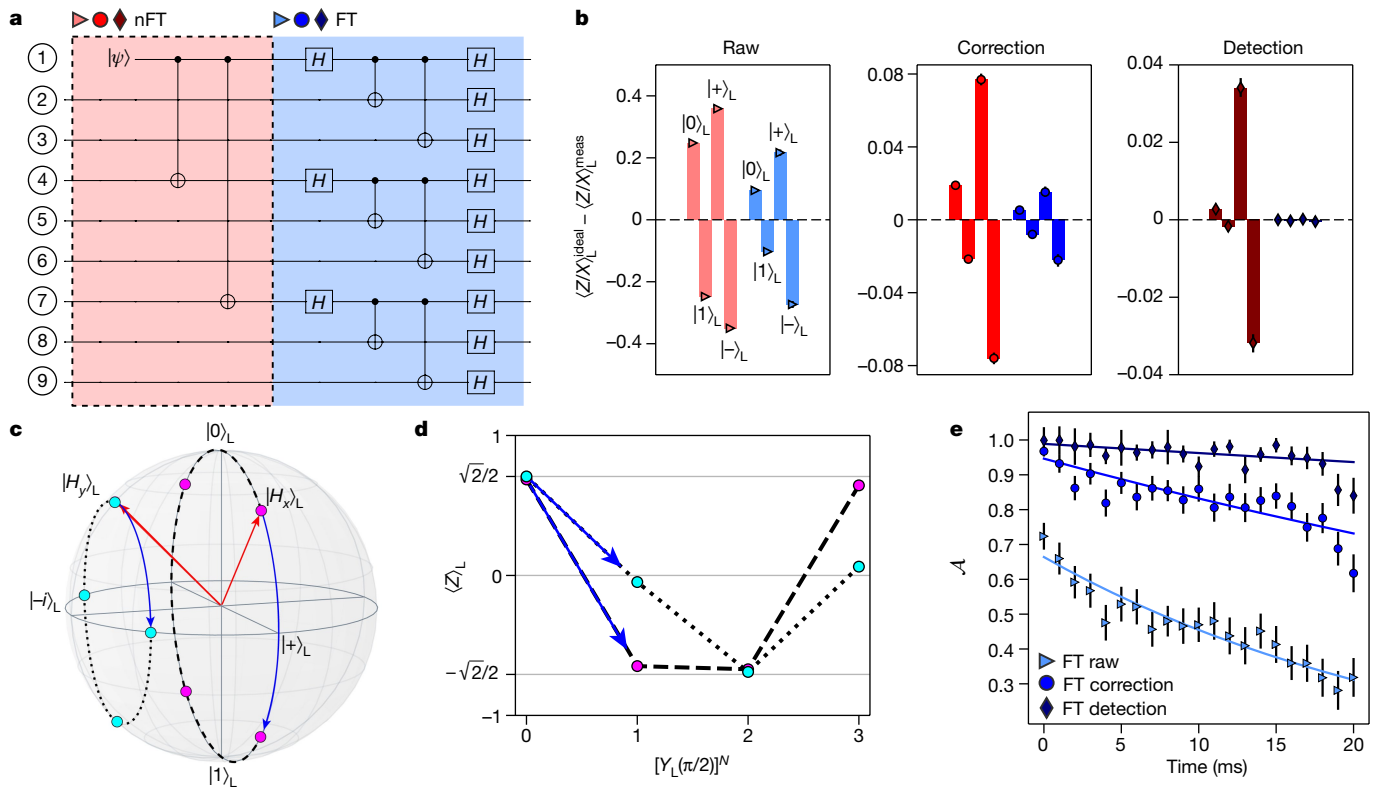


Fig. 2 | Fault-tolerant logical qubit-state preparation. **a**, Encoding circuit for creating logical qubit states. The right subcircuit (blue) is used for FT preparation of Z -logical basis states. X -logical basis states can be created by omitting the final Hadamard gates. The left subcircuit (red, dashed) can be optionally prepended for nFT preparation of arbitrary logical states. **b**, Errors for the key basis states of the encoded logical qubit. The measured expectation value of the parity ($\langle Z/X \rangle_L^{\text{meas}}$) is compared against the ideal parity of the logical state ($\langle Z/X \rangle_L^{\text{ideal}} = \pm 1$). Error bars indicate the 95% binomial proportion confidence interval. **c**, Magic states $|H_x\rangle_L$ (magenta) and $|H_y\rangle_L$ (cyan) are directly encoded using the full nFT circuit from **a** (red arrows). Subsequent $Y_L(\pi/2)$ rotations

and allows the possibility of early errors spreading between the separate GHZ states. As a consequence, this circuit loses the FT properties of the X - and Z -basis preparation circuits. To directly investigate the properties of FT, we compare the encoding performance of the right FT subcircuit to the full nFT circuit with $|\psi\rangle \in \{|0\rangle, |1\rangle, |+\rangle, |-\rangle\}$.

After measuring the data qubits, the logical measurement outcome is determined by calculating the total parity of all the data qubits in the Z basis, $Z_L = Z_1 Z_2 \dots Z_8 Z_9$. From equation (1), the $|0\rangle_L$ state has even parity ($\langle Z \rangle_L = 1$) whereas $|1\rangle_L$ has odd parity ($\langle Z \rangle_L = -1$). Similarly, the $|+\rangle$ / $|-\rangle_L$ states have even/odd parity in the X_L basis; a $Y_L(-\pi/2)$ operation following the encoding circuit, maps $\langle X \rangle_L \rightarrow \langle Z \rangle_L$. The measured raw parity compared with the ideal parity of each logical Z, X -basis state is presented in Fig. 2b. In addition to the total raw parity, Z_L , the data qubit measurements also provide the eigenvalues of the two stabilizers in the measurement basis. With this information, offline error correction can be applied, which yields an expected quadratic suppression of uncorrelated errors (that is, corrects any single error). Alternatively, error detection is performed by post-selecting experimental shots conditioned on the +1 eigenvalues of the stabilizers. This will yield an expected cubic suppression of uncorrelated errors (that is, detects any pair of errors). Further details of these protocols are given in Methods.

As shown in Fig. 2b, using the FT circuit (blue) and performing offline error correction, we prepare $|0\rangle_L, |1\rangle_L, |+\rangle_L$ and $|-\rangle_L$ states with errors of 0.27(4)%, 0.40(5)%, 0.76(7)% and 1.11(9)%, respectively. We note that the average state preparation and measurement error for a single physical qubit in the Z basis is 0.46(2)% (Supplementary Table 1) compared with

(blue arrows) are used to bound the fidelity. **d**, Experimental $\langle Z \rangle_L$ values for the states depicted in **c** after offline error correction. The 95% binomial proportion confidence intervals are smaller than the data points. **e**, Logical qubit coherence measured for the $|+\rangle_L$ state. After each wait time, a varying $Z(\phi)$ gate is applied to every data qubit, followed by $Y_L(-\pi/2)$. A fit of $\langle X \rangle_L$ depending on ϕ to a Ramsey fringe yields the Ramsey amplitude (\mathcal{A}). Error bars are the 95% confidence intervals from maximum likelihood estimation fits. The resulting contrast as a function of time is fit to a decaying exponential $\mathcal{A}e^{-t/T_2^*}$ for the raw, corrected and detected data. The fit parameters \mathcal{A} and T_2^* correspond to the Ramsey amplitude at $t=0$ and the $1/e$ coherence time, respectively.

0.33(5)% in the logical qubit. This is one context in which the logical qubit clearly outperforms our physical qubit. For the nFT circuit (red), the errors are 0.95(4)%, 1.08(4)%, 3.9(1)% and 3.8(1)%, respectively. The error-detection experiment presents particularly strong evidence for fault tolerance. We observe a remarkable gap in the failures between the nFT and FT protocols: over all the basis states, we see a total of 6 failures of FT error detection over 54,473 post-selected shots, compared with 430 failures over 50,372 post-selected shots when using nFT error detection. This agrees with a local error model where we expect cubic suppression of FT error detection, in stark contrast with nFT error detection, which can fail due to a single circuit fault. The observed two orders-of-magnitude difference lends further evidence that these circuits, which are fault tolerant in principle, are also fault tolerant in practice.

The nFT preparation circuit can also be used to create $|H_x\rangle_L = e^{-i\pi Y/8}|0\rangle_L$ and $|H_y\rangle_L = e^{-i\pi X/8}|0\rangle_L$ magic states, which can be distilled to implement FT non-Clifford gates^{7,45}. Figure 2c depicts these states on the logical Bloch sphere, and the results are shown in Fig. 2d. After offline error correction, the calculated $|H_x\rangle_L$ encoding fidelity is 97(1)% (Supplementary Table 2), which is above the distillation threshold of 92.4% (ref. 45).

The performance of the logical qubit as a quantum memory can be characterized by measuring the coherence of $|+\rangle_L$ versus time. The results of this logical T_2^* experiment are presented in Fig. 2e. For the raw, error-correction and error-detection decoding schemes, we measure a T_2^* of 26(2) ms, 78(9) ms and 370(160) ms. The measured T_2^* of each independent GHZ state in the logical qubit is almost entirely explained by the measured $T_2 = 0.6(1)$ s of the individual physical qubits

(Supplementary Figs. 7, 9). Future work that utilizes the gauge degrees of freedom to embed decoherence-free subspaces could dramatically improve performance^{46–48}. In this case, three-qubit antiferromagnetic GHZ states should readily extend the logical T_2^+ to the physical T_2^+ . Ultimately, repeated stabilization of the logical qubit over intermediate timescales will be required to achieve a robust quantum memory.

Logical gates

We implement a $Y_L(\theta)$ rotation on the encoded qubit, which can only be performed transversally for a discrete set of angles⁴⁹. For the Bacon–Shor code, the smallest transversal $Y_L(\theta)$ rotation available is $Y_L(\pi/2)$, which is generated by applying a physical $Y(\pi/2)$ to each data qubit, followed by relabelling the data qubit indices in post-processing (blue, Fig. 3a, b). We compare the performance of this FT rotation with a nFT circuit, which implements $Y_L(\theta) = Y_1 Z_2 Z_3 X_4 X_7(\theta)$ (red, Fig. 3a, c). In a perfect system, these rotations are equivalent for $\theta = N\pi/2, N \in \mathbb{Z}$ on the logical qubit, but differ in their operation on the gauge qubits. The nFT gate (Fig. 3) generates entanglement among the separate GHZ states, and so the failure of a single operation in the circuit can lead to the failure of the logical qubit.

The results of these different gate operations on the logical qubit are shown in Fig. 3d, e. The gate error per $\pi/2$ angle, corresponding to fit parameter Γ , is 0.3(1)% for the FT gate after offline error correction. This error rate explains the additional error present for the $|+\rangle_L$ states in Fig. 2b, which require two additional $Y_L(\pi/2)$ gates for state preparation and measurement. The remaining fit values are tabulated in Supplementary, Tables 3, 4. The error at $\theta = \pi$, the maximum gate angle required with optimized circuit compilation, is shown in Fig. 3e. The error for the FT gates and nFT continuous rotations is 0.4(2)% and 6.8(1.6)%, respectively, after offline error correction. Compared with the FT circuit, offline error correction on the nFT rotation provides minimal gains, indicative of a high proportion of weight-two errors relative to weight-one errors. In contrast, $\langle Z \rangle_L$ recovers quite substantially after error detection, indicating that there are still few weight-three or higher errors in the system. This is a striking example of the value of fault tolerance, which minimizes the impact of correlated weight-two errors on the logical qubit.

Stabilizer measurements

In stabilizer measurements, fault tolerance is achieved by a specific ordering of the interactions between the ancilla and the stabilizer block⁴¹. We insert a variable $Z(\theta)$ error on the ancilla during the measurement of a single stabilizer ($X_1 X_2 X_4 X_5 X_7 X_8$) and compare the impact of this error in a FT ordering and an nFT ordering. Without correction, a Z error on the ancilla qubit will propagate to an X error on the data qubit and flip $\langle Z \rangle_L$.

The results of this experiment are shown in Fig. 4a. At the extreme case of $\theta = \pi$, the raw parity is nearly identical in the two cases, but after offline error correction, the FT stabilizer measurement recovers the correct logical parity whereas the nFT stabilizer measurement induces a logical fault. This is because the FT gate ordering propagates a correlated error that decomposes as the product of (at worst) a single qubit fault and a benign transformation of the gauge subsystem⁴¹. By comparison, the nFT gate ordering propagates a correlated error that directly corrupts the logical subsystem.

At $\theta = 0$, (that is, when no error is added) the error rates with offline error correction for $|0\rangle_L$ after the nFT and FT stabilizer measurement are 0.85(23)% and 0.25(14)%, respectively, compared with a baseline $|0\rangle_L$ encoding error of 0.23(13)%. To within statistical error, there is no distinction between performing the FT stabilizer measurement or not, providing strong evidence that this procedure does not corrupt the logical qubit state beyond the error-handling capabilities of the code. However, there is a statistical separation ($P < 0.01$) between the nFT and FT ordering, with an average four-times reduction in error for this particular comparison. Although the nFT ordering is always

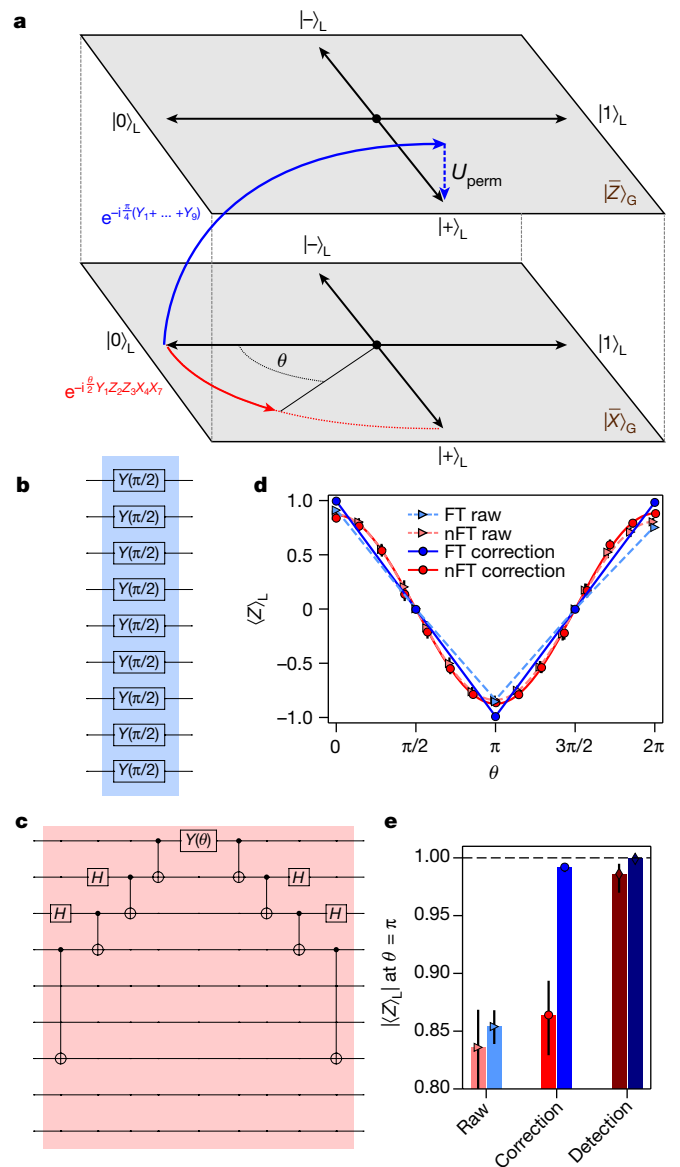


Fig. 3 | Manipulating logical states. **a**, A schematic depicting different logical operations. An FT discrete logical rotation (blue) operating on $|0\rangle_L$ is a transversal operation, $Y_L(\pi/2) = Y(\pi/2)^{\otimes 9}$ that leaves the code subspace (grey planes) and returns via a permutation of qubit labeling (U_{perm}). An nFT continuous logical rotation (red) operating on $|0\rangle_L$ is a five-qubit entangling operation, $Y_L(\theta) = Y_1 Z_2 Z_3 X_4 X_7(\theta)$ that rotates through the code subspace. At $\theta = \pi/2$, these gates are equivalent up to a gauge transformation. **b**, The circuit for the FT gate shown by the blue curve in **a**. **c**, The circuit for the nFT gate capable of creating any state along the red curve in **a**. **d**, Experimental results comparing FT (blue) and nFT (red) logical operations. The expectation value of the logical Z operator is fit to a decaying sinusoid $\langle Z \rangle_L = A \cos(\theta) e^{-\Gamma \theta / \pi}$. **e**, Detailed view at $\theta = \pi$. The error bars in **d**, **e** are 95% confidence intervals from the binomial distribution.

expected to perform worse, the error rate is still less than 1%, implying that the native Z -type errors on the ancilla qubit are quite small in this system (about 50 mrad per XX gate). Although this experiment is specific to X errors propagated from the X -stabilizer ancilla qubit, we also characterize Z errors with a similar experiment on the $|+\rangle_L$ state (Supplementary, Table 5).

In Fig. 4b, we show the results of directly measuring the full set of stabilizers with four additional ancilla qubits. First, the state is fault-tolerantly encoded into the $|0\rangle_L$ state. Then, an artificial error is

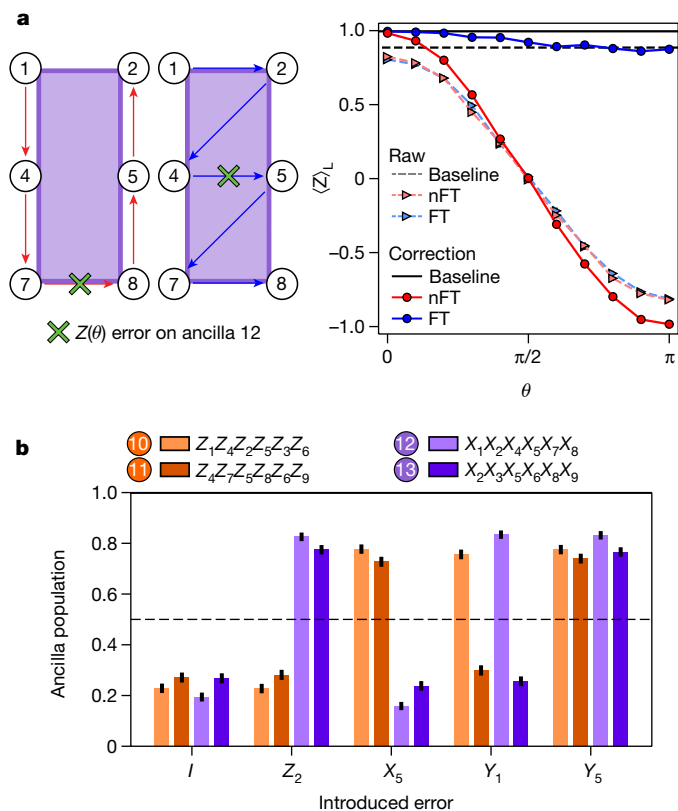


Fig. 4 | Detection of arbitrary single-qubit errors. **a**, Expectation value of the logical Z operator after encoding $|0\rangle_L$ (baseline, grey/black line), and then performing the nFT (red) or FT measurement (blue) of a single X -type stabilizer with a $Z(\theta)$ error inserted on the ancilla during measurement. **b**, After encoding $|0\rangle_L$, different Pauli errors are purposely introduced on a selected data qubit in the code. The identity operator (I) corresponds to the case where no artificial error is introduced. To detect an error, each stabilizer eigenvalue is mapped onto the state of the corresponding ancilla qubit. The ideal ancilla population is 0/1 depending on whether an error did not/did anticommute with the stabilizer block. The coloured bars correspond to the measured population of the different ancilla qubits. The error bars in **a**, **b** indicate the 95% binomial proportion confidence interval. The circuits used to generate the data shown in this figure are given in Extended Data Fig. 1.

applied to a data qubit. Finally, the full set of stabilizers, in sequential order X and then Z , are mapped to the ancilla qubits in a single shot. If no error has occurred, all four stabilizers commute with the logical qubit state and the ancilla qubits should remain in the $|0\rangle$ state. Conversely, if an error did occur on a data qubit, the stabilizers that do not commute with that error flip the state of the ancilla to $|1\rangle$. For example, a Pauli- Y error on data qubit 1 anticommutes with both the X and Z stabilizers that measure it, resulting in a flip of ancilla qubits 10 and 12, as we observe in the data. This confirms our ability to, on average, simultaneously identify arbitrary single-qubit errors along both X and Z axes using the stabilizer outcomes.

The data presented in Fig. 4b represent a sample of selected errors; the full dataset is available in Supplementary Fig. 10). Averaged over all the injected errors, the measured ancilla qubits 12, 13, 10 and 11 (in order of measurement) differ from the expected value by 17.9(3)%, 24.8(3)%, 24.4(3)% and 29.8(6)%, respectively. Most of this non-artificial error is induced by the syndrome extraction circuit itself. In particular, these results are well explained by the 3.8(2)% raw $|0\rangle_L$ encoding error, 6.9(5)% error per X stabilizer, 6.4(7)% error per Z stabilizer and a fixed 7.2(5)% Z -type error on the logical qubit that is consistent with the expected raw T_2^* decay over the 3-ms time required to measure X stabilizers, as shown in Fig. 2c.

Outlook

We have demonstrated fault-tolerant control of a logical qubit capable of correcting all single-qubit errors. There are two clear and immediate milestones ahead. One is to demonstrate a transversal CNOT logical gate between two logical qubits. This experiment should be possible in the current system given that two-qubit gates on 23 data qubits have recently been demonstrated⁵⁰. The other is to stabilize the state over multiple rounds of error correction, which can be achieved by breaking the ion chain to perform mid-circuit detection⁵¹. This shuttling will almost certainly require sympathetic cooling schemes, which have been previously demonstrated^{52,53} and can also be readily implemented in this system⁵⁰. In the longer-term, further improvements to the two-qubit gate fidelity will be required to achieve the pseudo-threshold where the logical qubit outperforms the physical qubit⁴⁰.

Online content

Any methods, additional references, Nature Research reporting summaries, source data, extended data, supplementary information, acknowledgements, peer review information; details of author contributions and competing interests; and statements of data and code availability are available at <https://doi.org/10.1038/s41586-021-03928-y>.

- Shor, P. W. Scheme for reducing decoherence in quantum computer memory. *Phys. Rev. A* **52**, R2493 (1995).
- Knill, E. & Laflamme, R. Theory of quantum error-correcting codes. *Phys. Rev. A* **55**, 900–911 (1997).
- Shor, P. W. Fault-tolerant quantum computation. In *Proc. 37th Conference on Foundations of Computer Science* (1996).
- Knill, E., Laflamme, R. & Zurek, W. Threshold accuracy for quantum computation. Preprint at <https://arxiv.org/abs/quant-ph/9610011> (1996).
- Gottesman, D. Theory of fault-tolerant quantum computation. *Phys. Rev. A* **57**, 127–137 (1998).
- Aharonov, D. & Ben-Or, M. Fault-tolerant quantum computation with constant error rate. *SIAM J. Comput.* (2008).
- Bravyi, S. & Kitaev, A. Universal quantum computation with ideal Clifford gates and noisy ancillas. *Phys. Rev. A* **71**, 022316 (2005).
- Feynman, R. P. Quantum mechanical computers. *Found. Phys.* **16**, 507–531 (1986).
- Abrams, D. S. & Lloyd, S. Simulation of many-body Fermi systems on a universal quantum computer. *Phys. Rev. Lett.* **79**, 2586–2589 (1997).
- Aspuru-Guzik, A., Dutoi, A. D., Love, P. J. & Head-Gordon, M. Simulated quantum computation of molecular energies. *Science* **309**, 1704–1707 (2005).
- Reiher, M., Wiebe, N., Svore, K. M., Wecker, D. & Troyer, M. Elucidating reaction mechanisms on quantum computers. *Proc. Natl Acad. Sci. USA* **114**, 7555–7560 (2017).
- Shor, P. W. Polynomial-time algorithms for prime factorization and discrete logarithms on a quantum computer. *SIAM Rev.* **41**, 303–332 (1999).
- Von Burg, V. et al. Quantum computing enhanced computational catalysis. Preprint at <https://arxiv.org/abs/2007.14460> (2020).
- Gidney, C. & Ekerå, M. How to factor 2048 bit RSA integers in 8 hours using 20 million noisy qubits. Preprint at <https://arxiv.org/abs/1905.09749> (2019).
- Gottesman, D. E. *Stabilizer Codes and Quantum Error Correction*. PhD thesis, California Institute of Technology (1997).
- Córcoles, A. D. et al. Demonstration of a quantum error detection code using a square lattice of four superconducting qubits. *Nat. Commun.* **6**, 6979 (2015).
- Takita, M., Cross, A. W., Córcoles, A. D., Chow, J. M. & Gambetta, J. M. Experimental demonstration of fault-tolerant state preparation with superconducting qubits. *Phys. Rev. Lett.* **119**, 180501 (2017).
- Linke, N. M. et al. Fault-tolerant quantum error detection. *Sci. Adv.* **3**, e1701074 (2017).
- Harper, R. & Flammia, S. T. Fault-tolerant logical gates in the IBM quantum experience. *Phys. Rev. Lett.* **122**, 080504 (2019).
- Andersen, C. K. et al. Repeated quantum error detection in a surface code. *Nat. Phys.* **16**, 875–880 (2020).
- Cory, D. G. et al. Experimental quantum error correction. *Phys. Rev. Lett.* **81**, 2152–2155 (1998).
- Chiaverini, J. et al. Realization of quantum error correction. *Nature* **432**, 602–605 (2004).
- Schindler, P. et al. Experimental repetitive quantum error correction. *Science* **332**, 1059–1061 (2011).
- Reed, M. D. et al. Realization of three-qubit quantum error correction with superconducting circuits. *Nature* **482**, 382–385 (2012).
- Riste, D. et al. Detecting bit-flip errors in a logical qubit using stabilizer measurements. *Nat. Commun.* **6**, 6983 (2015).
- Kelly, J. et al. State preservation by repetitive error detection in a superconducting quantum circuit. *Nature* **519**, 66–69 (2015).
- Gong, M. et al. Experimental verification of five-qubit quantum error correction with superconducting qubits. Preprint at <https://arxiv.org/abs/1907.04507> (2019).
- Nigg, D. et al. Quantum computations on a topologically encoded qubit. *Science* **345**, 302–305 (2014).

29. Luo, Y. H. et al. Quantum teleportation of physical qubits into logical code-spaces. Preprint at <https://arxiv.org/abs/2009.06242> (2020).
30. Heeres, R. W. et al. Implementing a universal gate set on a logical qubit encoded in an oscillator. *Nat. Commun.* **8**, 94 (2017).
31. Flühmann, C. et al. Encoding a qubit in a trapped-ion mechanical oscillator. *Nature* **566**, 513–517 (2019).
32. Ofek, N. et al. Extending the lifetime of a quantum bit with error correction in superconducting circuits. *Nature* **536**, 441–445 (2016).
33. Campagne-Ibarcq, P. et al. Quantum error correction of a qubit encoded in grid states of an oscillator. *Nature* **584**, 368–372 (2020).
34. de Neeve, B., Nguyen, T. L., Behrle, T. & Home, J. Error correction of a logical grid state qubit by dissipative pumping. Preprint at <https://arxiv.org/abs/2010.09681> (2020).
35. Wilhelm Maunz, P. L. *High Optical Access Trap 2.0* Report No. SAND2016-0796R (Sandia National Laboratories, 2016).
36. Debnath, S. et al. Demonstration of a small programmable quantum computer with atomic qubits. *Nature* **563**, 63–66 (2016).
37. Wright, K. et al. Benchmarking an 11-qubit quantum computer. *Nat. Commun.* **10**, 5464 (2019).
38. Bacon, D. Operator quantum error-correcting subsystems for self-correcting quantum memories. *Phys. Rev. A* **73**, 012340 (2006).
39. Aliferis, P. & Cross, A. W. Subsystem fault tolerance with the Bacon–Shor code. *Phys. Rev. Lett.* **98**, 220502 (2007).
40. Debroy, D. M., Li, M., Huang, S. & Brown, K. R. Logical performance of 9 qubit compass codes in ion traps with crosstalk errors. *Quantum Sci. Technol.* **5**, 034002 (2020).
41. Li, M., Miller, D. & Brown, K. R. Direct measurement of Bacon–Shor code stabilizers. *Phys. Rev. A* **98**, 050301 (2018).
42. Terhal, B. M. Quantum error correction for quantum memories. *Rev. Mod. Phys.* **87**, 307–346 (2015).
43. Dennis, E., Kitaev, A., Landahl, A. & Preskill, J. Topological quantum memory. *J. Math. Phys.* **43**, 4452–4505 (2002).
44. Li, M., Miller, D., Newman, M., Wu, Y. & Brown, K. R. 2D compass codes. *Phys. Rev.* **9**, 021041 (2019).
45. Reichardt, B. W. Quantum universality from magic states distillation applied to CSS codes. *Quantum Inf. Process.* **4**, 251–264 (2005).
46. Lidar, D. A., Chuang, I. L. & Whaley, K. B. Decoherence-free subspaces for quantum computation. *Phys. Rev. Lett.* **81**, 2594–2597 (1998).
47. Kielpinski, D. et al. A decoherence-free quantum memory using trapped ions. *Science* **291**, 1013–1015 (2001).
48. Hu, J., Liang, Q., Rengaswamy, N. & Calderbank, R. Mitigating coherent noise by balancing weight-2z-stabilizers. Preprint at <https://arxiv.org/abs/2011.00197> (2020).
49. Eastin, B. & Knill, E. Restrictions on transversal encoded quantum gate sets. *Phys. Rev. Lett.* **102**, 110502 (2009).
50. Cetina, M. et al. Quantum gates on individually-addressed atomic qubits subject to noisy transverse motion. Preprint at <https://arxiv.org/abs/2007.06768> (2020).
51. Kielpinski, D., Monroe, C. & Wineland, D. J. Architecture for a large-scale ion-trap quantum computer. *Nature* **417**, 709–711 (2002).
52. Home, J. P. et al. Complete methods set for scalable ion trap quantum information processing. *Science* **325**, 1227–1230 (2009).
53. Pino, J. M. et al. Demonstration of the QCCD trapped-ion quantum computer architecture. Preprint at <https://arxiv.org/abs/2003.01293> (2020).

Publisher's note Springer Nature remains neutral with regard to jurisdictional claims in published maps and institutional affiliations.

© The Author(s), under exclusive licence to Springer Nature Limited 2021

Methods

Experimental implementation

Each physical qubit is encoded in the $^2S_{1/2}$ electronic ground-state hyperfine ‘clock’ states of a single $^{171}\text{Yb}^+$ ion, $|0\rangle \equiv |F=0; m_F=0\rangle$ and $|1\rangle \equiv |F=1; m_F=0\rangle$, with a qubit frequency splitting of $\omega_0 = 2\pi \times 12.642820424(4)$ GHz. The qubits have a measured T_2 decoherence time in excess of 2.75 s (limited by the stability of external magnetic fields) and average single-shot detection fidelity of more than 99.5%. At the start of each experiment, the qubits are initialized to the $|0\rangle$ state. A given circuit is executed by sending appropriate signals to the AOM that implement single and two-qubit gates on the ion chain with all-to-all connectivity^{36,37}. At the end of a circuit, we perform global-state readout by simultaneously collecting state-dependent fluorescence from each ion using high-resolution optics and 32 individual photo-multiplier tubes.

We trap $^{171}\text{Yb}^+$ ions in a microfabricated-chip ion trap (High Optical Access 2.1.1 from Sandia National Labs) driven by a radiofrequency voltage at a frequency of 36.06 MHz. We define the x axis along the trap axis, with the z axis perpendicular to the chip surface. A magnetic field of 5.183 G along the z axis defines the atomic quantization axis. The individually addressing (global) Raman beam is oriented along the z (y) axis of the trap, so that the Raman process transfers momentum to the ions along the $\hat{y} - \hat{z}$ direction. We selectively couple light to the lower-frequency set of radial modes by tilting the trap principal axes using a static electric $y-z$ quadrupole. We use quadratic and quartic axial potentials to minimize the spacing inhomogeneity for the middle thirteen ions. In the 15-ion chain, the longest wavelength (in-phase) mode along each trap axis is $(\nu_x, \nu_{y-z}, \nu_{y+z}) = (0.193, 3.077, 3.234)$ MHz.

An imaging objective with numerical aperture of 0.63 (Photon Gear) is used to focus each of the 32 individual beams to a waist of 0.85 μm , spaced by 4.43 μm at the ions. The mode-locked 355-nm laser (Coherent Paladin 355-4000) used to drive Raman transitions has been modified to tune the repetition rate of the laser to null the four-photon cross-beam Stark shift. Typical spin-flip Rabi frequencies achieved in our system are 500 kHz. The maximum crosstalk on nearby ions is 2.5% of the Rabi frequency of the addressed ion.

Before each experiment, the ions are cooled to near the motional ground state through a combination of Doppler cooling and Raman side-band cooling and then initialized into $|0\rangle$ via optical pumping. After the circuit, resonant 369-nm light on the $^2S_{1/2} \rightarrow ^2P_{1/2}$ cycling transition is used to perform state detection. Scattered light is collected through the 0.63-numerical-aperture objective and imaged with magnification of 28 onto a multimode (100- μm core) fibre array that is broken out into individual photo-multiplier tubes (Hamamatsu H10682). About 1% of the total light is detected as counts. Dark/bright states are mapped to $|0\rangle/|1\rangle$ states by setting a threshold at more than one photon detected within a detection window (typically 100 μs). State preparation and detection errors are 0.22(2)% and 0.71(4)% for $|0\rangle$ and $|1\rangle$, respectively. Detection crosstalk onto neighbouring channels is 0.3(2)%; see Supplementary Table 1 for detailed error budget.

The entire experiment is controlled by an field-programmable gate array (Xilinx) programmed via the ARTIQ software. Radiofrequency gate waveforms are generated by a four-channel arbitrary waveform generator (Keysight M3202A), one of which drives the global beam, and two of which are routed through a custom switch network onto any of the 15 middle channels of the individual beam AOM at each timestep in the circuit.

Native ion-trap single-qubit gates

The native physical single-qubit gate available to our system is a single-qubit rotation about a vector in the $x-y$ plane, $R(\theta, \phi)$ where θ is the angle of rotation and ϕ is the angle between the rotation axis and the x axis. In this notation, $RX(\theta) = R(\theta, 0)$ and $RY(\theta) = R(\theta, \pi/2)$. In addition, we use compound SK1 pulses to suppress angle and cross-talk errors⁵⁴. The SK1 pulses are shaped with a smooth Gaussian amplitude envelope to avoid frequency content that may excite axial motion due

to light-induced prompt charge effects from partially exposed semiconductor in the chip trap. Owing to hardware limitations, single-qubit gates are run sequentially. We implement virtual $RZ(\theta)$ gates via a software advance of the local oscillator phase, tracked for each individual ion. Before each circuit is run, we calibrate the amplitude of an $RX(\theta)$ on each qubit in the chain. We achieve single-qubit native gate error rates of $1.8(3) \times 10^{-4}$ on a 15-ion chain as measured by randomized benchmarking (Supplementary Fig. 1).

Native ion-trap two-qubit gates

The native two-qubit operation is the $XX(\theta)$ Ising gate, implemented via a Mølmer-Sørensen interaction⁵⁵. CNOT gates can be constructed from an $XX(\pi/4)$ gate and additional single-qubit gates⁵⁶. Offline, we calculate laser-pulse solutions for XX gates to disentangle the motional modes using amplitude-modulated waveforms³⁶ discretized into 16 segments with linear interpolation between segments to avoid undesirable excitation of the axial motion. In an equispaced chain of 15 ions, we observe that the middle 11 radial motional modes are also roughly equispaced. The laser detuning from motional modes is constant across the waveform and is chosen to sit approximately halfway between two adjacent modes, which leads to particularly simple laser waveforms to eliminate qubit-motion entanglement at the end of the gate. The gate frequency for a particular gate pair is optimized to minimize the required laser power, minimize sensitivity to mode-frequency errors of less than 1 kHz, and to avoid coupling to modes with low spatial frequencies that are subject to heating. Gate durations are 225 μs . To avoid unwanted couplings, we run two-qubit gates sequentially. Before a batch of circuits is run, we calibrate the amplitude, common phase and differential phase of each gate in the circuit. We achieve between 98.5% and 99.3% fidelity on a typical gate, measured by parity fringes after a varying odd number of successive non-echoed or echoed XX gates (Supplementary Fig. 2).

Error-correction protocol

Global measurement at the end of each circuit provides the state of all nine data qubits. From this data, we can calculate the raw total parity, $Z_L = Z_1 Z_2 \dots Z_8 Z_9$, and the eigenvalue of the two Z stabilizers, $S_1 = Z_1 Z_4 Z_2 Z_3 Z_7 Z_6$ and $S_2 = Z_4 Z_7 Z_5 Z_8 Z_6 Z_9$. The stabilizer eigenvalues can be used to produce an offline correction, or as flags to discard datasets in the case of error detection. The processed total parity, Z'_L , from the different protocols is then given by the following logic: **Raw**, $Z'_L = Z_L$; **Error Correction**, if $S_1 = -1 \parallel S_2 = -1$, then $Z'_L = -Z_L$, else $Z'_L = Z_L$; **Error Detection**, if $S_1 = -1 \parallel S_2 = -1$, then *Discard Data*, else $Z'_L = Z_L$.

Data availability

The data that support the findings of this study are available from the corresponding author upon request. Source data are provided with this paper.

Code availability

The code used for the analyses is available from the corresponding author upon request.

54. Brown, K. R., Harrow, A. W. & Chuang, I. L. Arbitrarily accurate composite pulse sequences. *Phys. Rev. A* **70**, 052318 (2004).
55. Mølmer, K. & Sørensen, A. Multiparticle entanglement of hot trapped ions. *Phys. Rev. Lett.* **82**, 1835–1838 (1999).
56. Maslov, D. Basic circuit compilation techniques for an ion-trap quantum machine. *New J. Phys.* **19**, 023035 (2017).

Acknowledgements This work was performed at the University of Maryland with no material support from IonQ. We acknowledge discussions with N. M. Linke and the contributions of J. Mizrahi, K. Hudek, J. Amini, K. Beck and M. Goldman to the experimental setup. This work is supported by the ARO through the IARPA LogiQ programme, the NSF STAQ Program, the

Article

AFOSR MURIs on Dissipation Engineering in Open Quantum Systems and Quantum Interactive Protocols for Quantum Computation, and the ARO MURI on Modular Quantum Circuits. L.E. and D.M.D. are also funded by NSF award DMR-1747426.

Author contributions L.E. collected and analysed the data. L.E., D.M.D., C.N. and M.N. wrote the manuscript and designed figures. M.C. and C.M. led construction of the experimental apparatus with contributions from L.E., C.N., A.R., D.Z. and D.B. Theory support was provided by D.M.D., M.N., M.L. and K.R.B. C.M. and K.R.B. supervised the project. All authors discussed results and contributed to the manuscript.

Competing interests K.R.B. is a scientific advisor for IonQ, Inc. and has a personal financial interest in the company.

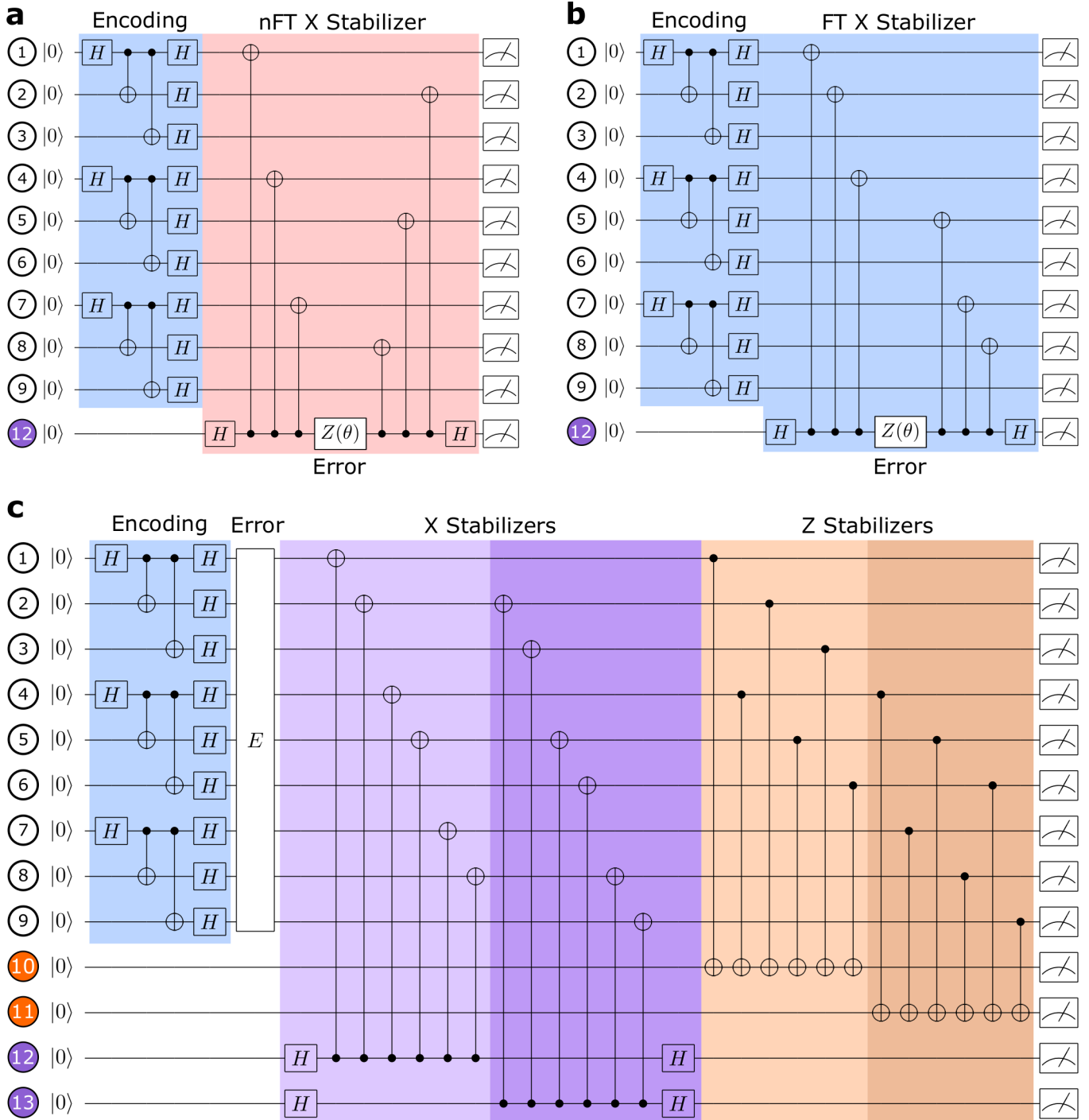
Additional information

Supplementary information The online version contains supplementary material available at <https://doi.org/10.1038/s41586-021-03928-y>.

Correspondence and requests for materials should be addressed to Laird Egan.

Peer review information *Nature* thanks Daniel Gottesman, Jonathan Home, Philipp Schindler and the other, anonymous, reviewer(s) for their contribution to the peer review of this work.

Reprints and permissions information is available at <http://www.nature.com/reprints>.



Extended Data Fig. 1 | Stabilizer measurement circuits. a, b, Non-fault-tolerant (a, red, right) and fault-tolerant (b, blue, right) stabilizer measurement orderings, performed on a FT-encoded $|0\rangle_L$ state (a, b, blue, left). In both cases, a variable error $Z(\theta)$ is introduced on the ancilla qubit in the middle of the stabilizer measurement operation. These circuits were used to generate

the data in Fig. 2a. c, Direct measurement of the full error syndrome. Various single-qubit 'errors' are introduced on any one of the data qubits to generate different ancilla measurement outcomes. This circuit was used to generate the data in Fig. 2b.